# CMOS-Compatible Carbon Dioxide Sensors


**Zeyu Cai, Robert van Veldhoven, Hilco Suy, Ger de Graaf, Kofi A. A. Makinwa, and Michiel Pertijs**

## 1 Introduction

$CO_2$ sensors can provide important information for indoor air-quality monitoring, given that $CO_2$ concentration in the air is highly correlated with the occupancy of a building [1]. As this increases, human-related pollutants such as bacteria, molds, and volatile organic compounds also increase, meaning a heightened risk for the health of the occupants. On the other hand, the more people there are in a building, the higher the $CO_2$ concentration will be as a by-product of human respiration, implying that $CO_2$ concentration can be used as an indicator for air quality. To do so, concentrations of up to 2500 ppm need to be measured with a resolution of better than 200 ppm [1]. Currently available sensors that meet these requirements are optical sensors based on nondispersive infrared absorption (NDIR) [2–4]. Despite their merits of being accurate and selective, optical $CO_2$ sensors also have several considerable downsides. They require a cavity or tube for optical waveguiding, making them relatively bulky and expensive. Moreover, the infrared source typically consumes a significant amount of power [2–4].

Z. Cai (✉)
Delft University of Technology, Delft, The Netherlands

NXP Semiconductors, Eindhoven, The Netherlands
e-mail: zeyu.cai@nxp.com

R. van Veldhoven
NXP Semiconductors, Eindhoven, The Netherlands

H. Suy
ams AG, Eindhoven, The Netherlands

G. de Graaf · K. A. A. Makinwa · M. Pertijs
Delft University of Technology, Delft, The Netherlands



K. A. A. Makinwa et al. (eds.), *Low-Power Analog Techniques, Sensors for Mobile Devices, and Energy Efficient Amplifiers*,
https://doi.org/10.1007/978-3-319-97870-3_11

Alternatively, $CO_2$ concentration can be determined indirectly by measuring the thermal conductivity (TC) of the air [5–8]. This approach exploits the fact that the TC of $CO_2$ is lower than that of the other constituents of air, and thus the thermal conductivity of the air is $CO_2$ dependent. Therefore, when a resistive transducer is suspended in ambient air and heated up, its temperature rise is $CO_2$ dependent. This temperature rise can be detected as a change of the transducer's electrical resistance. Since the required transducer can be realized with minimum post-processing in standard CMOS technology, this approach has important cost and miniaturization advantages compared to NDIR-based sensors. However, as the difference in the thermal conductivities of the air and $CO_2$ is very small, tiny changes in resistance need to be sensed (e.g., 1.5 μΩ change per ppm change in $CO_2$), making the measurement extremely demanding [5].

To perform accurate measurement, a proper reference must be chosen. Furthermore, the dynamic range (DR) requirement of the readout circuit must be significantly reduced to achieve energy-efficient measurements. This chapter presents two different designs, implemented in the amplitude domain and time domain, respectively. In the first approach [5], the steady-state temperature rise and power dissipation of the transducer are measured relative to those of a capped reference transducer. The sensor achieves a $CO_2$ resolution of about 200 ppm (1 σ) in a measurement time of 30 s. In the time-domain approach [9], the $CO_2$-dependent thermal time constant is measured using a low-noise PDΔΣM. This sensor achieves a $CO_2$ resolution of 94 ppm while dissipating only 12 mJ per measurement, which is best in class in both resolution and energy consumption for $CO_2$ sensors in CMOS technology.

This chapter is organized as follows: The analysis, design, and measurement results of the amplitude-domain approach will be introduced in Sect. 2. The operating principle and design of the time-domain approach are explained in Sect. 3, together with its measurement results. The pros and cons of these two approaches are analyzed in Sect. 4 and the chapter ends with conclusions in Sect. 5.

## 2 $CO_2$ Sensor Based on Amplitude-Domain TC Measurement

### *2.1 Operating Principle*

#### 2.1.1 Thermal Resistance Measurement Using a Resistive Transducer

Figure 1a shows a hot-wire resistive transducer realized in a VIA layer in the metal stack of a standard CMOS process. When power is dissipated in such a transducer, it loses heat through two main paths, both of which can be modeled as thermal resistances, as shown in Fig. 1b: one to the surrounding air ($R_{th\_air}$) and the other to the substrate through the anchor points ($R_{th\_sub}$). The temperature rise ($\Delta T$) of the transducer relative to the ambient temperature ($T_{amb.}$) caused by the power

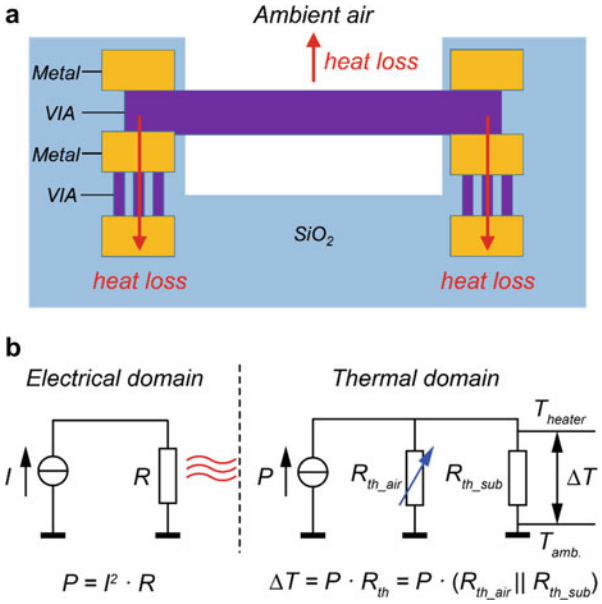


**Fig. 1** Amplitude-domain TC sensing principle: (**a**) cross-sectional view of a suspended hot-wire resistive transducer and its heat loss paths; (**b**) the equivalent model in both electrical and thermal domains [5] (reproduced with permission)

dissipated in the transducer ($P$) is directly proportional to the parallel combination $R_{\text{th}}$ of $R_{\text{th\_air}}$ and $R_{\text{th\_sub}}$:

$$\Delta T = P \cdot R_{\text{th}} = P \cdot \left(R_{\text{th\_air}} \parallel R_{\text{th\_sub}}\right) \tag{1}$$

Since the TC of $CO_2$ is lower than that of the other constituents of air, $R_{\text{th\_air}}$ is $CO_2$ dependent, and so $\Delta T$ can be used to determine the $CO_2$ concentration in air. To maximize sensitivity, heat loss to the substrate must be minimized, which is usually achieved by employing suspended transducers [10, 11], realized in our case by a single release etch step.

While $\Delta T$ in (1) can be measured using a dedicated temperature sensor (e.g., thermopiles; [7]), the use of the electrical resistance of the heater to measure its temperature greatly simplifies the fabrication process, allowing a single resistive transducer to be used as a heater, as shown in Fig. 1a [12].

To a good approximation, the resistance of the tungsten transducer is a linear function of temperature:

$$R = R_0 \cdot (1 + \alpha \cdot (T - T_0)) \tag{2}$$

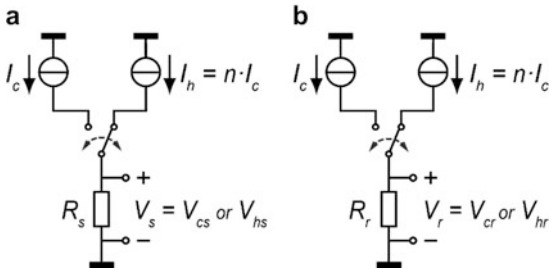


**Fig. 2** (**a**) $CO_2$-sensitive and (**b**) reference transducer alternately biased at two different current levels [5] (reproduced with permission)

where $R_0$ is the nominal electrical resistance of the transducer at room temperature $T_0$ and α its temperature coefficient. For our transducers, the nominal resistance $R_0$ and temperature coefficient α are 110 Ω and 0.0017/K, respectively. The nominal resistance $R_0$ is set by the aspect ratio of the resistor and was designed to allow sufficient power to be dissipated in the resistor at the available voltage headroom.

To generate $\Delta T$, the transducer is alternately biased at a low current $I_c$ and a high current $I_h$ (Fig. 2a) corresponding to a "cold" and a "hot" state. The power dissipation in (1) then becomes the difference in power dissipation between these two states ($\Delta P$), and $R_{th}$ becomes:

$$R_{th} = \frac{\Delta T}{\Delta P} = \frac{T_h - T_c}{P_h - P_c} = \frac{R_h - R_c}{R_0 \alpha \left(I_h^2 R_h - I_c^2 R_c\right)} \tag{3}$$

In order to accurately measure $R_{th}$, both $\Delta T$ and $\Delta P$ need to be accurately measured. The nominal $R_{th}$ of our tungsten transducer (i.e., at 400 ppm $CO_2$ and 25 °C) is about 53,500 K/W. A change of 200 ppm $CO_2$ results in about 80 ppm change in the thermal resistance of air. Taking account of the substrate heat loss, a 200 ppm change in $CO_2$ only corresponds to a relative change of $R_{th}$ of about 50 ppm. This implies that the power levels and temperature measurement should be stable to within ±25 ppm, making the measurement very challenging.

### 2.1.2 Ratiometric Thermal Resistance Measurement

Measuring the thermal resistance of a $CO_2$-sensitive transducer relative to that of a ($CO_2$ insensitive) reference transducer, rather than measuring the absolute thermal resistance of one transducer, greatly relaxes the power stability and temperature measurement requirements, as the absolute accuracy requirement is replaced by a matching requirement of the $CO_2$-sensitive and reference transducers. The reference transducer is biased in the same way as the sensitive transducer (Fig. 2b). Their thermal-resistance ratio can be derived from (3) and expressed as a multiplication of two ratios: the ratio of the temperature difference of the sensitive transducer ($\Delta T_s$)

and the temperature difference of the reference transducer ($\Delta T_r$) and the ratio of their power differences ($\Delta P_r/\Delta P_s$):

$$\frac{R_{ths}}{R_{thr}} = \left(\frac{\Delta T_s}{\Delta T_r}\right)\left(\frac{\Delta P_r}{\Delta P_s}\right) = \left(\frac{R_{hs}-R_{cs}}{R_{hr}-R_{cr}}\right)\left(\frac{n^2 I_c^2 R_{hr} - I_c^2 R_{cr}}{n^2 I_c^2 R_{hs} - I_c^2 R_{cs}}\right) = \left(\frac{V_{hs}-nV_{cs}}{V_{hr}-nV_{cr}}\right)\left(\frac{nV_{hr}-V_{cr}}{nV_{hs}-V_{cs}}\right) \quad (4)$$

where $n = I_h/I_c$, $V_{hs} = n \cdot I_c \cdot R_{hs}$, $V_{cs} = I_c \cdot R_{cs}$, $V_{hr} = n \cdot I_c \cdot R_{hr}$, $V_{cr} = I_c \cdot R_{cr}$, and the transducers are assumed to have identical $R_0$ and $\alpha$, which therefore cancel out. The last term in (4) shows that the thermal-resistance ratio can be written as a product of two voltage-difference ratios, which in this work are digitized sequentially by a dual-mode switched-capacitor incremental $\Delta\Sigma$ ADC and multiplied in the digital backend.

### 2.1.3 Ratiometric Readout with Transducer Pairs

With the sequential readout of hot and cold states, the voltage drop across the transducers varies significantly between the two states. Consequently, to avoid clipping, the following ADC must have a large dynamic range. To relax the dynamic range, a pair of $CO_2$-sensitive transducers ($R_{s1}$, $R_{s2}$) and a pair of reference transducers ($R_{r1}$, $R_{r2}$) are employed (Fig. 3).

Package-level sealing ensures that both reference transducers are isolated from the ambient air. In each pair, the transducers are alternately biased at $I_c$ and $I_h = n \cdot I_c$, generating simultaneously "hot" and "cold" voltages for both sensitive ($V_{hs}$, $V_{cs}$)

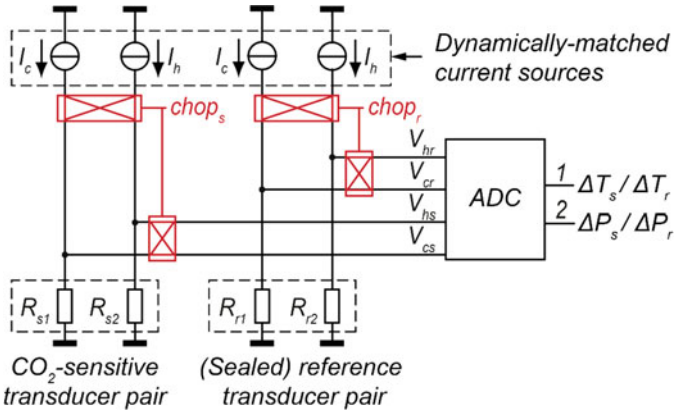


**Fig. 3** Block diagram of the ratiometric thermal-conductivity sensor readout with transducer pairs for baseline-resistance cancellation [5] (reproduced with permission)

and reference transducers ($V_{hr}$, $V_{cr}$). The current ratio $n$ is chosen to optimize the signal-to-noise ratio (SNR). For a given power consumed in biasing the transducers, a smaller $n$ gives smaller signal amplitude, while a larger $n$ reduces the current in the "cold" state, thereby increasing the noise level associated with that state. Therefore, SNR degrades for small and large values of $n$ and an optimum can be found for which the SNR is maximized. A parametric simulation of our design shows that this optimum is reached at a ratio of $n = 5$. Mismatches are averaged out, as the transducers in each pair are periodically swapped by the chopper switches around them. The "hot" and "cold" voltages are simultaneously sampled by scaled switched-capacitor circuits and merged together (detailed in the next subsection).

## *2.2 Design and Implementation*

### 2.2.1 Charge-Balancing Incremental ΔΣ Modulator

To obtain a $CO_2$-sensing resolution of the order of 200 ppm (corresponding to 50 ppm or 14.3 bits resolution in the $R_{th}$ ratio), we digitize each of the voltage ratios in (4) with a resolution better than 15.3 bits (equivalent to 100 ppm $CO_2$). An incremental delta-sigma ADC is suitable, as $CO_2$ concentration tends to change relatively slowly. A charge-balancing $\Delta\Sigma$ modulator is used that operates in two modes: temperature mode and power mode. First, in temperature mode, it produces a bitstream *bs* proportional to the first voltage ratio in (4), which equals the temperature-difference ratio. Then, in power mode, it produces a bitstream proportional to the second voltage ratio in (4), which equals the power-difference ratio. These bitstreams are decimated by an off-chip decimation filter and the results are multiplied in the digital domain to obtain the thermal-resistance ratio.

Figure 4 shows the switched-capacitor implementation of the modulator. It consists of a switched-capacitor integrator, with four parallel input branches connecting to the four transducers and a clocked comparator. The sample and hold circuit uses a double-sampling scheme, which doubles the signal amplitude compared to the single-sampling scheme used in [12]. The integrator employs a gain-boosted folded-cascode OTA with a unity-gain bandwidth of about 2.5 MHz and a nominal DC gain of 140 dB, to make sure that the settling is accurate and to prevent integrator leakage from limiting the resolution [13]. The comparator is a latched comparator using a preamplifier to reduce the kick-back effect of the positive feedback latch [14]. To minimize charge injection, minimum size switches ($W/L = 0.8\ \mu m/0.16\ \mu m$) are used. In order to obtain accurate $CO_2$ measurements, accurate matching is required for the capacitors, especially for the current sources.

### 2.2.2 Dynamically Matched Current Sources and Current Trimming

Errors in the 1:$n$ bias current ratio lead to errors in the measured $R_{th}$ ratio. According to system-level simulations, in order to reduce the resulting error in the measured

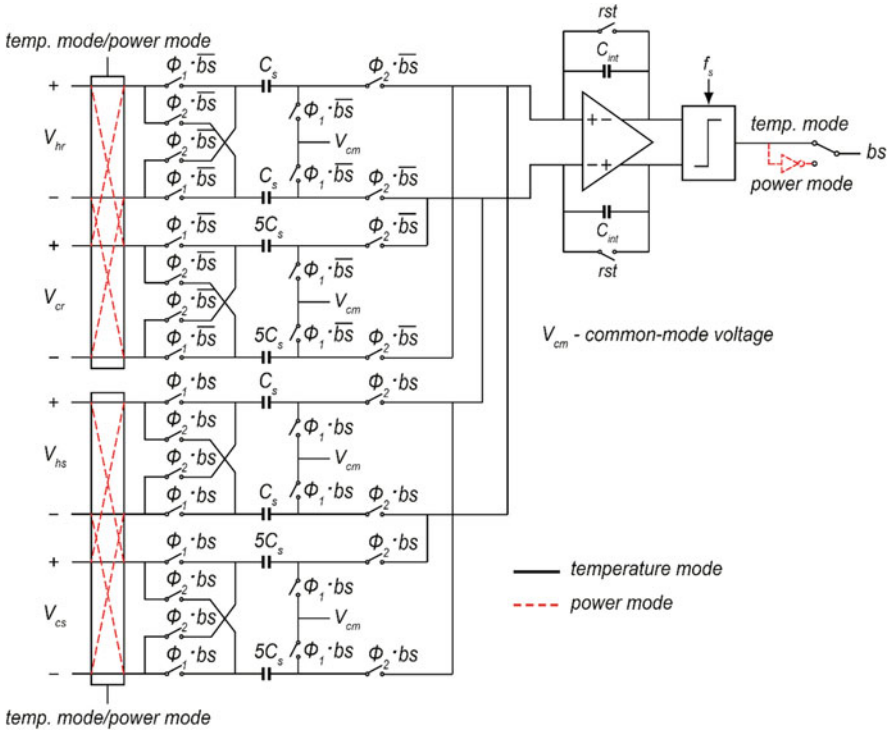


**Fig. 4** Simplified circuit diagram of the switched-capacitor delta-sigma modulator in both temperature and power modes [5] (reproduced with permission)

$CO_2$ concentration to less than 200 ppm by a one-point offset trim, the error in current ratio should be less than 0.06%. To achieve this, dynamic element matching (DEM) is applied (Fig. 5).

Each transducer is associated with a set of five unit-current sources, each of which can be connected to the transducer through a switch. These switches are digitally controlled according to the DEM timing diagram shown in Fig. 5. When one sensitive transducer is biased by all five unit current sources (in the hot state), the other sensitive transducer is sequentially biased by one unit current source (in the cold state), generating an accurate average current ratio of five. The same biasing approach is applied to the reference transducers. It should be noted that the current-domain chopping (indicated in Fig. 3) is also implemented by this switching scheme (switching between $I_c$ and $5I_c$).

In principle, the periodic chopping of the transducers modulates the errors due to transducer mismatch to an AC signal. However, it may still be necessary to trim the initial mismatch, so that the ripple caused by the mismatch at the output of the first integrator will not overload the $\Delta\Sigma$ modulator. As shown in Fig. 6, the two currents $I_{OUT1}$ and $I_{OUT2}$, biasing the sensitive transducers $R_{s1}$ and $R_{s2}$, are generated using

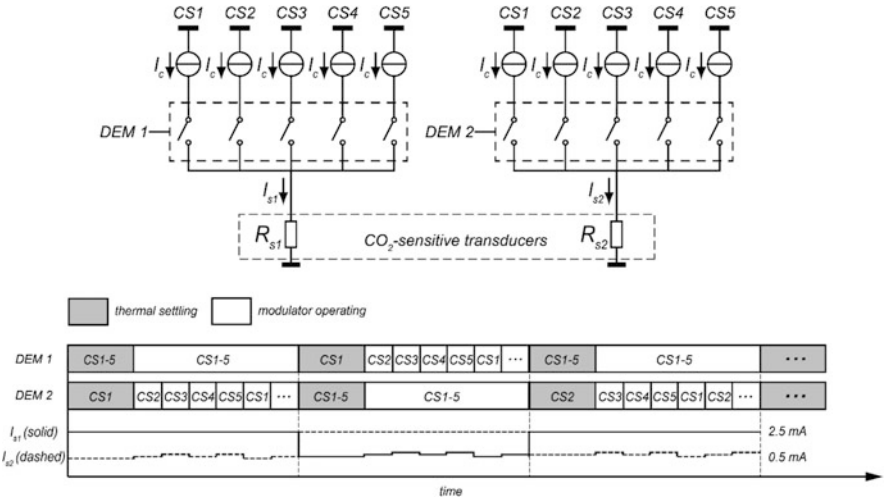


**Fig. 5** Dynamically matched current sources and associated timing diagram (same algorithm applies to the current sources for the reference transducers) [5] (reproduced with permission)

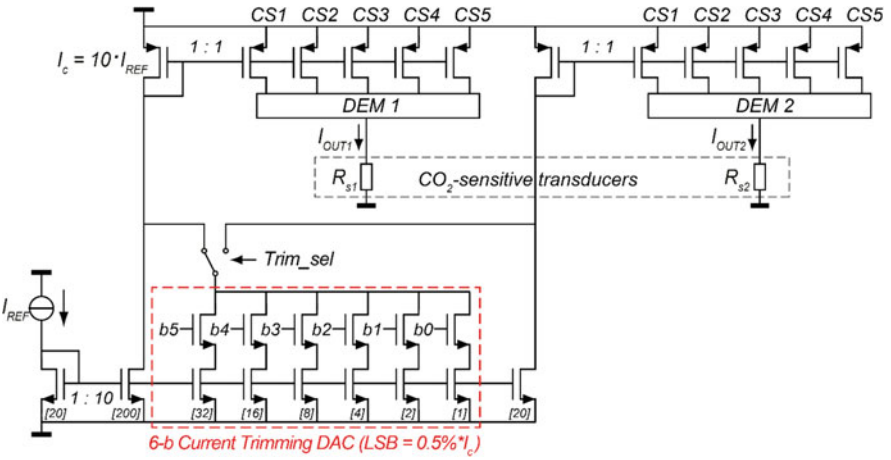


**Fig. 6** Circuit diagram of the current sources with a 6-bit current trimming DAC (LSB current = 0.5% × $I_c$; the current sources as well as the current trimming DAC for the reference transducers are identical, not shown here; cascode transistors omitted for simplicity) [5] (reproduced with permission)

PMOS current mirrors (an identical circuit, not shown, is used for the reference transducers). A 6-bit binary-weighted current DAC (LSB current = 0.5% · $I_c$), embedded in the current source circuit, is used to trim the input current of these current mirrors, thus effectively compensating for the resistance mismatch between $R_{s1}$ and $R_{s2}$. Note that the current ratio between $I_{OUT1}$ and $I_{OUT2}$ does not need to be accurate, as long as both $I_{OUT1}$ and $I_{OUT2}$ provide an accurate 1:$n$ current ratio

sequentially to the individual transducers, which is ensured by the current-source DEM (Fig. 5). In this way, the measured thermal-resistance ratio is a ratio between the averaged thermal resistances of the two sensitive transducers and that of the two reference transducers.

## 2.3 *Measurement Results*

The readout circuit as well as the tungsten-wire transducers have been designed and fabricated in 0.16 μm CMOS technology [5]. Figure 7 shows the layout plot and micrographs of the integrated readout circuit and one of the transducers. The active die area of the circuit equals 0.7 $mm^2$, of which 0.37 $mm^2$ is occupied by the current sources and 0.33 $mm^2$ by the switched-capacitor $\Delta\Sigma$ modulator. The transducers are on another chip for flexibility, fabricated using the same CMOS process followed by an etch step to release the wires.

To demonstrate the insensitivity of the ratiometric measurement to the absolute current and power levels, Fig. 8 shows the measured temperature, power, and

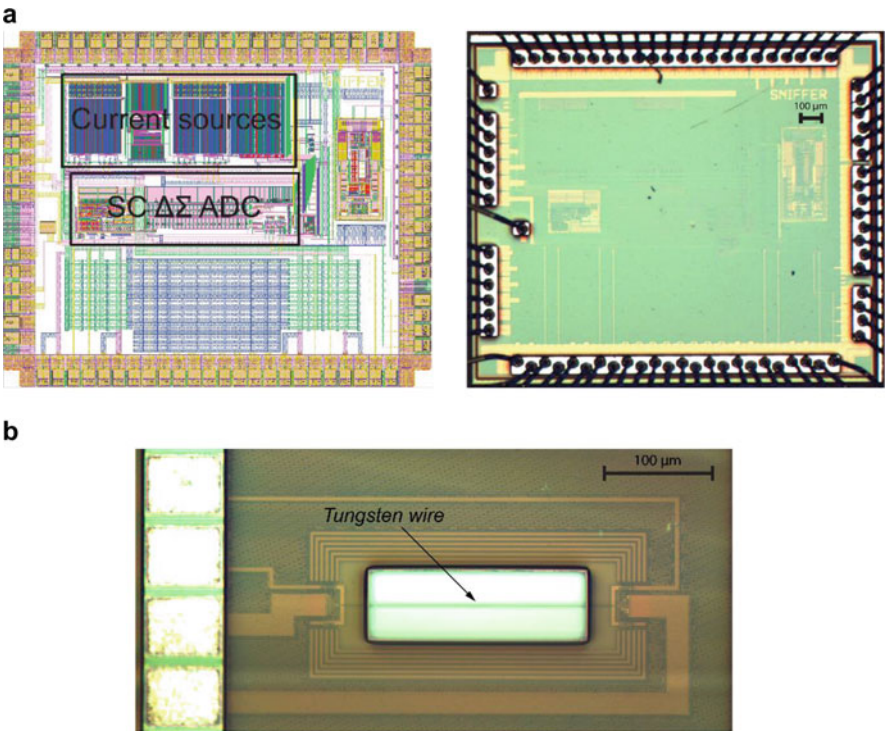


**Fig. 7** (**a**) Layout plot and micrograph of the integrated readout circuit and (**b**) micrograph of a CMOS-compatible tungsten-wire transducer [5] (reproduced with permission)

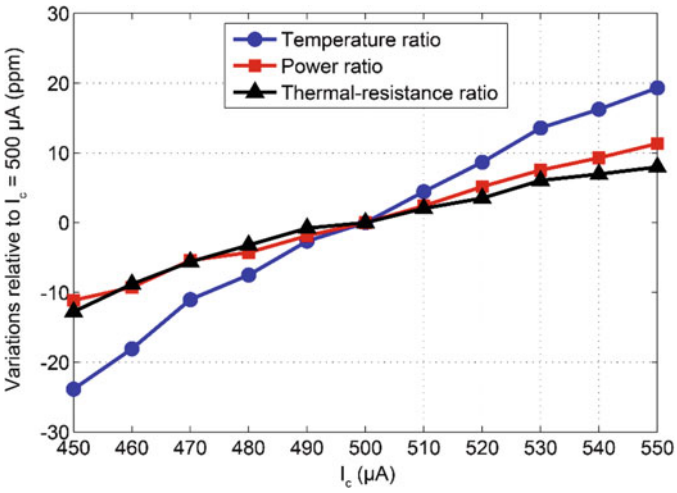


**Fig. 8** Variations in temperature, power, and thermal-resistance ratios between the sensitive and reference transducers as a function of the bias current at "cold" state ($I_c$) [5] (reproduced with permission)

thermal-resistance ratios as a function of $I_c$ (the bias current at the "cold" state). For a $\pm 10\%$ change in $I_c$, the power ratio only changes by about $\pm 10$ ppm. For our $CO_2$ sensor, a 200 ppm change in $CO_2$ will result in about a 50 ppm change in thermal-resistance ratio, which requires the errors of power ratio to be within 25 ppm. Thus, the measured results indicate that the ratiometric measurement effectively alleviates the dependence on the stability of the power dissipation. The measured thermal-resistance ratio also varies by about $\pm 10$ ppm, which could be due to the secondary temperature dependence of the thermal conductivity of air.

Figure 9 shows the thermal-resistance ratio of the tungsten transducers measured using the single-sampling readout circuit described in [12], while the $CO_2$ concentration was changed stepwise from 500 ppm to 9000 ppm. Like other TC-based $CO_2$ sensors [5–7], the readings of the sensor are affected by variations in ambient conditions, which need to be compensated for in a final product. In our experiment, ambient temperature, humidity, and pressure sensors were applied to facilitate cross-sensitivity compensation. To lower the noise level, a measurement time of 70 s was used for this experiment, at which the measured resolution is equivalent to 228 ppm $CO_2$ ($1\sigma$). The thermal-resistance ratio measured using the readout circuit has a sensitivity of 0.29 ppm/ppm $CO_2$, and shows good correlation with the $CO_2$ level measured using an NDIR-based reference sensor.

The improvement of the double-sampling readout circuit (Fig. 4) has also been validated with discrete heaters Figaro TGS-8100 [15]. These discrete devices have similar electrical and thermal properties to the tungsten transducers and are more readily sealed manually at the package level, so they are used here as a substitute for the tungsten transducers. The results are shown in Fig. 10. Four different $CO_2$ levels (500 ppm, 2500 ppm, 4500 ppm, 9000 ppm) and a baseline (pure

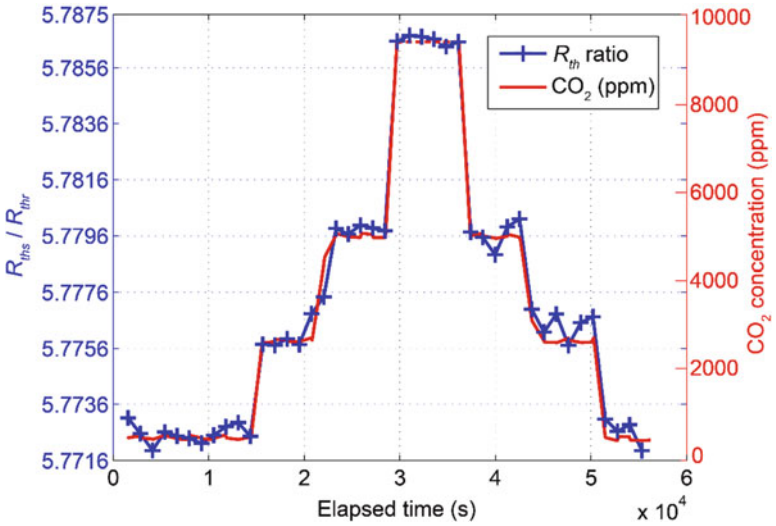


**Fig. 9** Thermal-resistance ratio measured using the tungsten-wire transducers in combination with the single-sampling readout circuit [12], for stepwise changing $CO_2$ concentration with compensation for temperature, humidity, and pressure cross-sensitivity, along with $CO_2$ concentration measured using an accurate reference NDIR sensor [2, 5] (reproduced with permission)

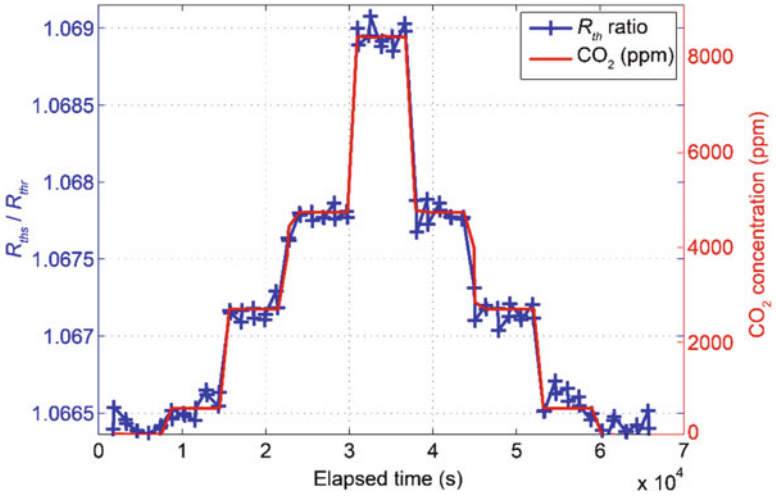


**Fig. 10** Thermal-resistance ratio measured using the double-sampling readout circuit (Fig. 4) in combination with Figaro TGS 8100 transducers, with compensation for temperature, humidity, and pressure cross-sensitivity, for stepwise changing $CO_2$ concentration, along with $CO_2$ concentration measured using an accurate reference NDIR sensor [2, 5] (reproduced with permission)

air) were used in this experiment. The thermal-resistance ratio measured has a sensitivity of 0.27 ppm/ppm $CO_2$, and shows good correlation with the reference $CO_2$ measurements. In these experiments, a measurement time of 30 s was used.

# 3 $CO_2$ Sensor Based on Time-Domain TC Measurement

## *3.1 Operating Principle*

### 3.1.1 Time-Domain TC Measurement

An alternative to measuring the steady-state temperature rise of a hot-wire is to characterize its thermal time constant $\tau_{th}$, which is the product of the wire's ambient thermal resistance ($R_{th}$) and its thermal capacitance ($C_{th}$) [6, 7, 16]. When the wire is driven with a current $I_d$ pulsed at a frequency $f_{drive}$ and is thus periodically heated, its temperature transients are delayed relative to the driving pulses. The delay is determined by the thermal time constant $\tau_{th}$, which in turn depends on the TC of the surrounding air (Fig. 11).

Such a TC sensor can be modeled as a first-order low-pass filter. Using a fixed driving frequency will then result in phase-delayed temperature transients relative to the driving pulses, from which $\tau_{th}$ can be derived. The optimal driving frequency equals the filter's pole frequency, i.e., $1/2\pi\tau_{th}$, at which the sensitivity of the phase shift to the changes of $\tau_{th}$ is maximized. For our devices, $\tau_{th} \approx 17$ μs, leading to an optimal $f_{drive}$ around 9–10 kHz.

Earlier TC sensors based on transient measurements use separate resistive heaters and temperature sensors, either thermistors [6] or thermopiles [17], which are

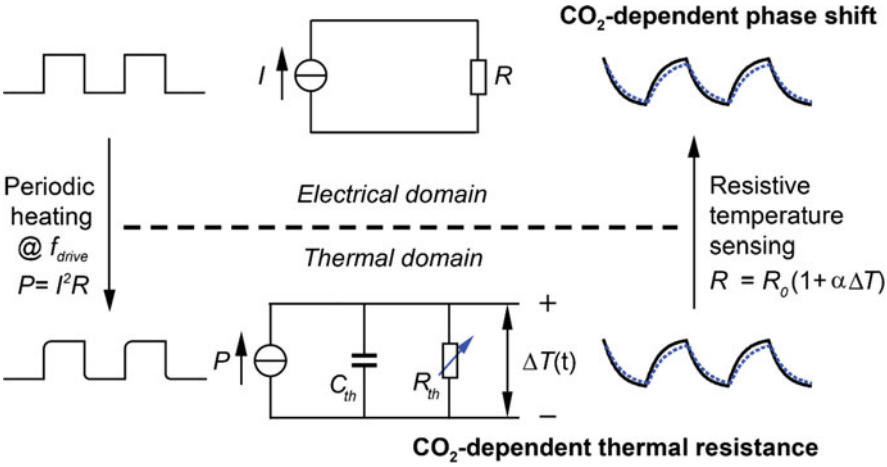


**Fig. 11** Transient thermal-resistance (thermal delay) measurement principle [9] (reproduced with permission)

mounted together on a thermally isolated membrane. This separates the temperature transients from the electrical transients and thus simplifies the readout at the cost of fabrication complexity and hence cost. Since resistive transducers can be used as both a heater and a temperature sensor, the heating and sensing functions can, in principle, be combined in a single resistor, provided an appropriate readout scheme is devised. This will challenge the design of the readout circuit but will greatly reduce the fabrication cost.

In earlier work, both a sine wave [6] and a square wave [17] were used to drive the heater. The benefit of sinusoidal driving is that it contains only a fundamental frequency without harmonics, and thus the readout circuit can directly measure the phase shift of the temperature signal by filtering and zero-crossing detection [6]. In contrast, a square-wave driving signal will generate a sinusoidal fundamental signal and a series of odd-order harmonics. The phase shift of the fundamental can be detected using synchronous detection [17]. In terms of circuit implementation, a square-wave excitation is much easier to generate than a sine wave. The phase-domain delta-sigma modulator (PDΔΣM) enables the use of square-wave excitation of the sensor [18, 19], which greatly simplifies the design of the driving source.

### 3.1.2 Phase-Domain Delta-Sigma Modulator

The phase shift $\phi_{\text{sig}}$ of the transducer's temperature when it is driven at $f_{\text{drive}}$ can be found by coherent detection, that is, by multiplying with a reference signal at the same frequency $f_{\text{drive}}$ with phase $\phi_{\text{ref}}$, as illustrated in Fig. 12a. Assuming sinusoidal

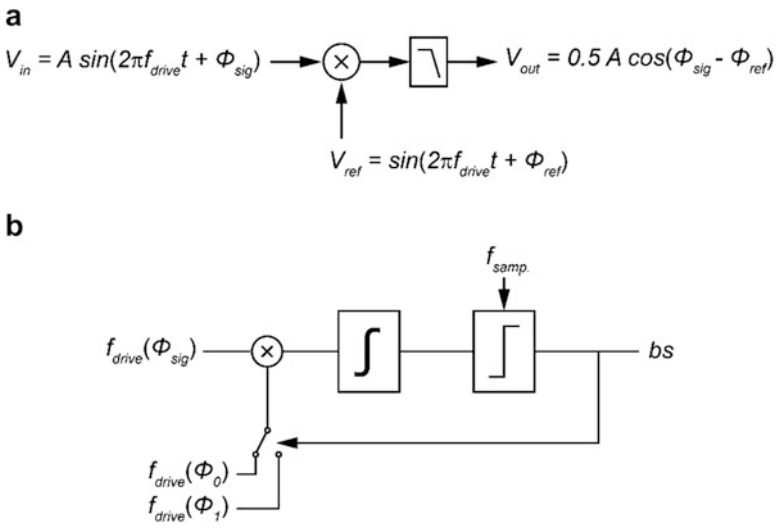


**Fig. 12** (**a**) Phase detection by means of coherent detection. (**b**) Phase detection using a delta-sigma feedback loop [9] (reproduced with permission)

signals for simplicity, the result is a DC component proportional to the cosine of the phase difference and a component at $2f_{\text{drive}}$ that can be removed by a low-pass filter:

$$\begin{aligned} &A \cdot \sin\left(2\pi f_{\text{drive}} t + \phi_{\text{sig}}\right) \cdot \sin\left(2\pi f_{\text{drive}} t + \phi_{\text{ref}}\right) = \\ &0.5 \cdot A \cdot \left[\cos\left(\phi_{\text{sig}} - \phi_{\text{ref}}\right) - \cos\left(4\pi f_{\text{drive}} t + \phi_{\text{sig}} + \phi_{\text{ref}}\right)\right] \end{aligned} \tag{5}$$

As shown in Fig. 12b, the coherent detector can be embedded in a delta-sigma ($\Delta\Sigma$) loop, where an integrator serves as a low-pass filter and feedback is applied in the phase domain, by toggling $\phi_{\text{ref}}$ between two phase references $\phi_0$ and $\phi_1$ depending on the bit-stream output *bs* [18, 19]. The feedback loop, on average, nulls the input of the integrator and thus ensures that the average phase reference tracks the phase of the input signal, which can therefore be derived from the average value of the bit-stream.

From (5), it can be seen that in order to allow the $\Delta\Sigma$ modulator to track $\phi_{\text{sig}}$, the reference phase $\phi_{\text{ref}}$ should toggle between two values such that the term $\cos(\phi_{\text{sig}} - \phi_{\text{ref}})$ presents inverse polarity. This implies that the two reference phases ($\phi_0$ and $\phi_1$) should be located on both sides of the 90° phase shift of the input signal. The resolution with which the phase shift can be determined depends on the number of clock cycles $N$ that the $\Delta\Sigma$ modulator is operated per measurement, that is, the oversampling ratio (OSR), and equals $(\phi_1 - \phi_0)/N$ for a first-order $\Delta\Sigma$ modulator [19].

Simulation shows that the phase shift induced by a 1 ppm change in $CO_2$ concentration is roughly 7 μ°. This can be used to estimate the required OSR to arrive at a desired $CO_2$ resolution. For example, for a full scale $\phi_0 - \phi_1 = 4°$, the required OSR for a quantization step equivalent to 100 ppm $CO_2$ is about 6000.

## *3.2 Design and Implementation*

### 3.2.1 Dynamic Range Requirement Reduction

While the voltage across the transducer in Fig. 11 contains temperature information, its sensitivity to temperature will change with the current level. To mitigate this, an additional sense current $I_s$, switched at a much faster rate $f_{\text{sense}}$, produces a modulated voltage proportional to $R(t)$ with a fixed sensitivity to temperature, independent of the drive current (Fig. 13a).

To make it easier to detect this voltage in the presence of the large voltage transients at $f_{\text{drive}}$ (about 300 mV peak-to-peak), a pair of transducers are heated simultaneously by pulsed currents $I_d$ (=2 mA) and read out differentially by out-of-phase sense currents $I_s$ (=0.5 mA), switched at $f_{\text{sense}} = 15 \times f_{\text{drive}}$ (Fig. 13b). Thus, the signal at $f_{\text{drive}}$ is converted into a common-mode signal and can be rejected by the differential readout circuit. Each transducer is also biased by an additional

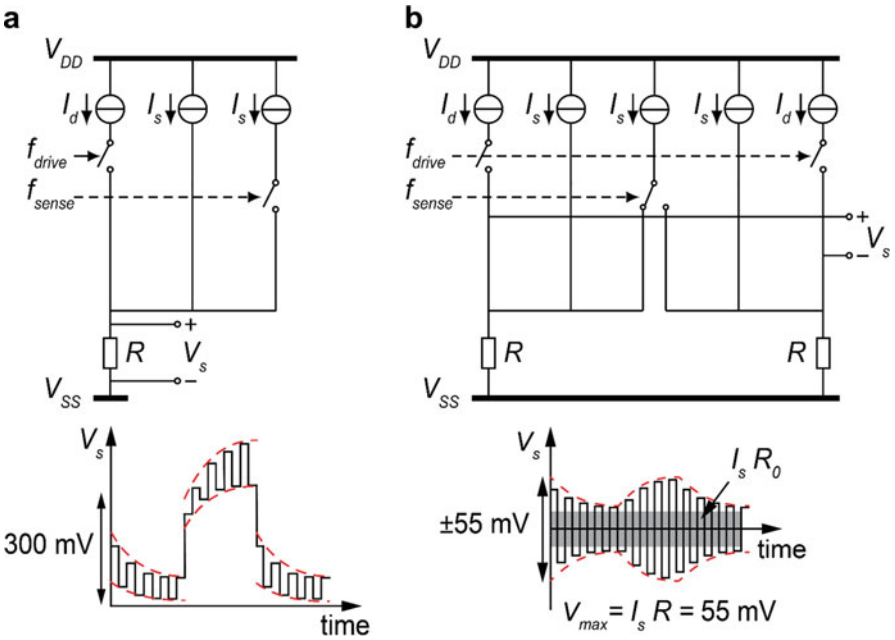


**Fig. 13** Sensing the temperature-induced resistance changes using (**a**) current modulation and (**b**) differential sensing

constant sense current $I_s$ (=0.5 mA) to provide a voltage signal to be sensed when $I_d$ is switched off.

An odd ratio of 15 between the $f_{sense}$ and $f_{drive}$ is chosen here to prevent errors due to the down conversion of harmonics of the drive signal. Due to mismatch of the drive signals, a fraction of the common-mode drive signal will be converted to a differential-mode signal. If $f_{sense}$ was an even multiple of $f_{drive}$, the odd harmonics of this differential-mode signal would be down converted to $f_{drive}$ by the chopper demodulation at $f_{sense}$, and would then be detected by the PD$\Delta\Sigma$M, affecting the decimated results. As $f_{sense}$ is chosen to be an odd multiple of $f_{drive}$, the down-converted harmonics end up at DC and are rejected by the PD$\Delta\Sigma$M.

Even with this arrangement, a large dynamic range is still required, since the temperature-induced resistance increase ($\Delta R \approx 3\ \Omega$) is small compared to the baseline resistance ($R_0 = 110\ \Omega$), while the variation in $\Delta R$ as a result of variations in $CO_2$ concentration is even smaller (about 1.5 $\mu\Omega$ per ppm $CO_2$). To cancel the voltage steps associated with $R_0$, two poly resistors $R_p$ ($= R_0$) are connected in series with the transducers and the sense currents are routed such that the additional voltage drop $I_s R_p$ cancels out $I_s R_0$ (Fig. 14). The remaining differential signal $V_s$ is ideally equal to $I_s\ \Delta R$ and reflects the transient temperature change, which is about 1.5 mV, 200× smaller than the initial 300 mV transients.

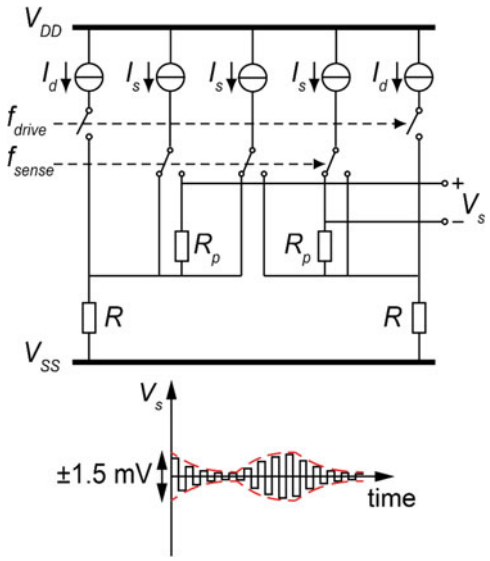


**Fig. 14** Baseline resistance compensation using a pair of poly resistors

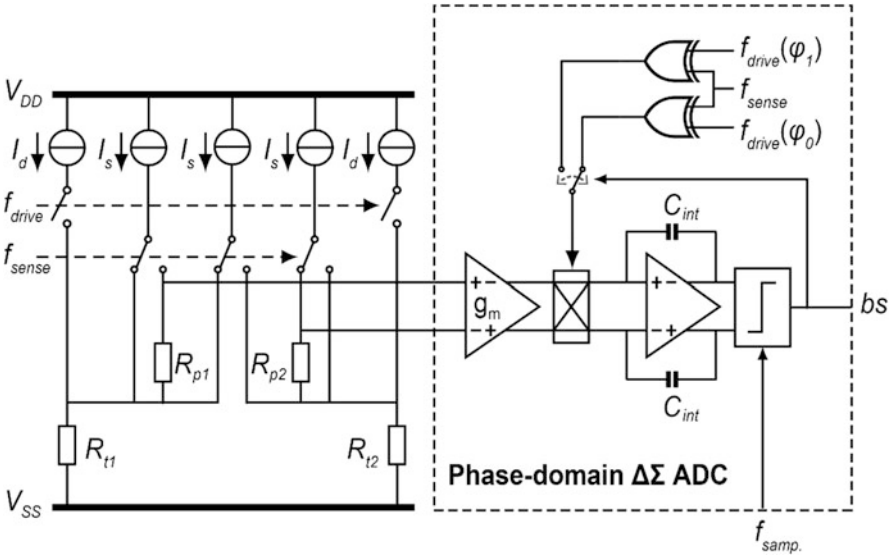


**Fig. 15** Circuit diagram of the proposed readout circuit [9] (reproduced with permission)

### 3.2.2 Phase-Domain Delta-Sigma Modulator

The phase shift of the temperature-related differential signal $V_s$ ($\approx I_s\,\Delta R$) is digitized by a low-noise phase-domain $\Delta\Sigma$ modulator similar to that described in [20]. As shown in Fig. 15, before demodulation by $f_{sense}$, a low-noise transconductor $g_m$ converts the differential voltage $V_s$ into a current. This current passes through a

chopper switch, which serves the dual purpose of demodulation by $f_{sense}$ (i.e., down converting the desired phase information at $f_{sense} + f_{drive}$ to $f_{drive}$), and multiplication with the phase-shifted versions of $f_{drive}$ as a function of the bit-stream (as in Fig. 12b). This combination is realized by multiplying the phase-shifted versions of $f_{drive}$ with $f_{sense}$ by means of XOR gates. The resulting demodulated current is proportional to the phase difference between $V_s(t)$ and the selected phase reference. This difference is integrated on capacitors $C_{int}$ of an active integrator and quantized using a clocked comparator to form a $\Delta\Sigma$ loop, which nulls the input of the integrator and thus ensures that the average phase reference tracks the phase of $V_s(t)$, which can therefore be derived from the average value of the bit-stream.

To ensure that the noise from the transconductor is lower than that from the transducer and its bias circuit, the $g_m$ of the transconductor should be at least 400 μS. The transconductance of the $g_m$ stage is about 560 μS. The sampling frequency is chosen to be the same as $f_{drive}$. Both $f_{drive}$ and $f_{sense}$, including the feedback signals at $f_{drive}$ with reference phases $\phi_0$ and $\phi_1$, are derived from a single off-chip master clock. The capacitor $C_{int}$ in the integrator is 50 pF.

### 3.3 *Measurement Results*

Both the transducers and the readout circuit have been implemented in the same 0.16 μm CMOS technology (Fig. 16), with an active area of 0.3 $mm^2$ and 3.14 $mm^2$, respectively [9]. For flexibility, they have been realized on separate chips and connected at the PCB level. The modulator's control signals were generated using

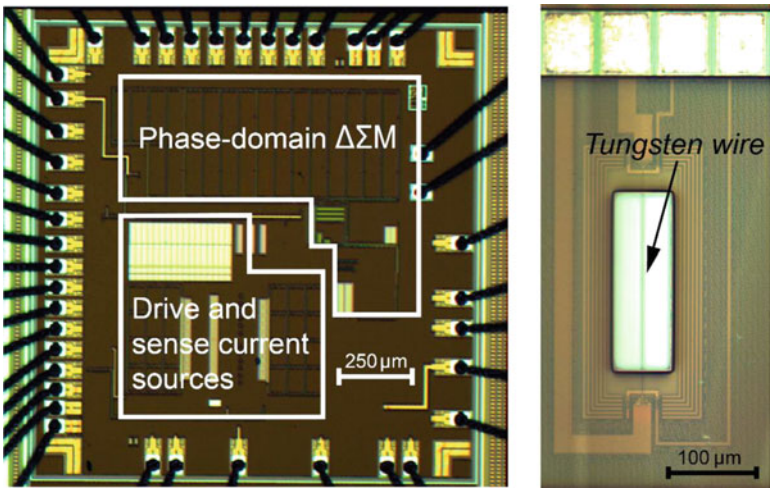


**Fig. 16** Micrograph of the readout circuit and the transducer [9] (reproduced with permission)

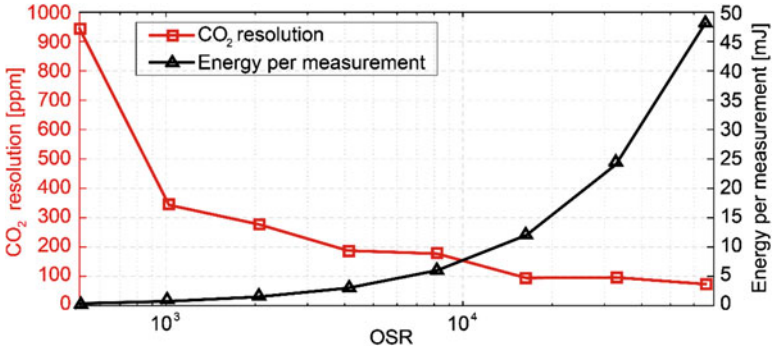


**Fig. 17** Measured resolution (standard deviation of 20 consecutive measurements) and energy per measurement as a function of OSR [9] (reproduced with permission)

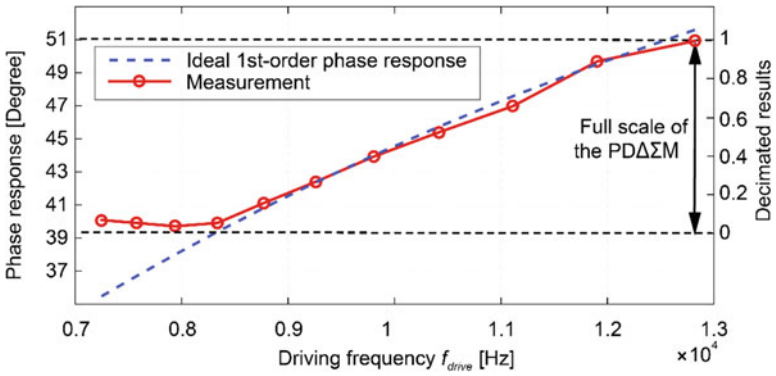


**Fig. 18** Measured phase shift as a function of the drive frequency [9] (reproduced with permission)

an FPGA. The readout circuit consumes 6.8 mW from a 1.8 V supply, 6.3 mW of which is dissipated in the transducers.

Figure 17 shows the measured resolution at different oversampling ratios (OSR). A resolution equivalent to 94 ppm $CO_2$ is reached at an OSR of 16,384, which corresponds to a measurement time of 1.8 s and an energy consumption of 12 mJ.

The thermal delay or equivalently the measured phase shift, caused by the thermal resistance and thermal capacitance, should present a first-order behavior as a function of the driving frequency, like a first-order electrical low-pass filter. This is confirmed by measurements shown in Fig. 18. The measured phase shift as a function of the drive frequency shows a good agreement with the ideal first-order behavior associated with the hot-wire's thermal time constant (measured using a larger full scale $\phi_0 - \phi_1 = 12°$ for clarity).

To measure its $CO_2$ response, the sensor was placed in a sealed box along with an NDIR reference $CO_2$ sensor [2]. As before, ambient temperature, humidity, and pressure sensors were placed in the box to facilitate cross-sensitivity compensation.

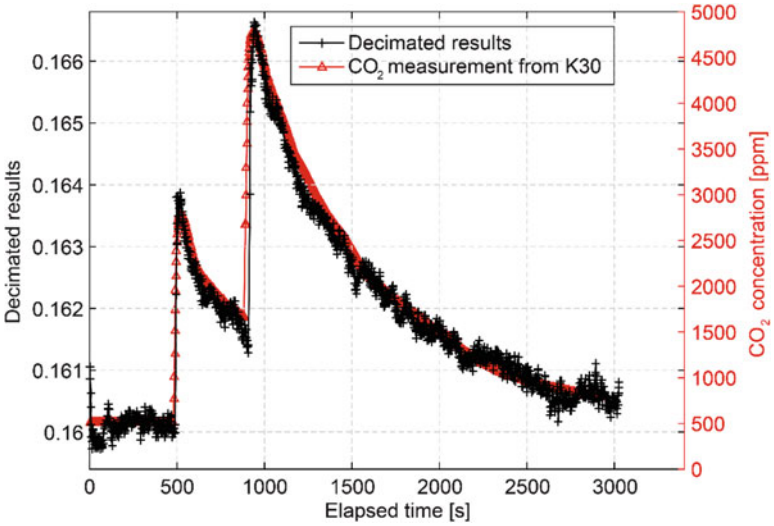


**Fig. 19** Transient $CO_2$ response of the $CO_2$ sensor and an NDIR-based reference sensor K30 [2, 9] (reproduced with permission)

Figure 19 shows the good agreement between the readings of our sensor and the $CO_2$ concentration measured by the reference sensor.

## 4 Comparison and Benchmarking

Table 1 summarizes the performance of the amplitude-domain and time-domain TC-based $CO_2$ sensors and compares it with prior works. The two sensors were implemented in the same CMOS technology and have similar chip areas. In both cases, most of the power is dissipated in the transducers for heating. The time-domain sensor consumes about half the average power of the amplitude-domain sensor due to the circumvention of the reference transducers. By moving the design from the amplitude domain to the time domain and using a PD$\Delta\Sigma$M based on a continuous-time $g_m$-$C$ integrator, the noise performance and the energy efficiency of the readout circuit have been greatly improved. The sensor based on time-domain TC measurement achieves a $CO_2$ resolution of 94 ppm while dissipating only 12 mJ per measurement, representing a significant improvement in energy efficiency compared to previously reported $CO_2$ sensors.

The attained results indicate that TC-based $CO_2$ sensors realized CMOS technology are a promising candidate for air-quality monitoring, provided they are cointegrated with appropriate sensors to compensate for the cross-sensitivity of TC measurement to temperature, humidity, and pressure. The resulting advantages in cost (>10×), volume (>100×), and energy consumption are significant, making them a promising candidate for $CO_2$ sensing in cost- and energy-constrained applications.

**Table 1** Performance summary of the amplitude-domain and time-domain TC-based $CO_2$ sensors and benchmarking

| Parameter | Time domain | Amplitude domain | [6] | [2] | [21] |
|---|---|---|---|---|---|
| Method | TC | TC | TC | NDIR | NDIR |
| Technology | CMOS (0.16 μm) | CMOS (0.16 μm) | SOI MEMS | Module | SOI MEMS |
| On-chip readout | Y | Y | N | N | N |
| Area (sensor) | 0.3 $mm^2$ | 0.6 $mm^2$ | 16 $mm^2$ | – | [a]0.3 $mm^2$ |
| Area (readout) | 3 $mm^2$ | 3 $mm^2$ | – | – | – |
| Supply voltage | 1.8 V | 1.8 V | – | 5–14 V | – |
| Power consumption | 6.8 mW | 11.2 mW | 3 mW | 200 mW | 200 mW |
| Meas. time | 1.8 s | 30 s | 60 s | 2 s | 2.4 s |
| $CO_2$ resolution | 94 ppm | 202 ppm | 456 ppm | 20 ppm | 250 ppm |
| Energy/meas. | 12 mJ | 336 mJ | 180 mJ | 400 mJ | 480 mJ |

[a]Area of the IR emitter only, excluding 80 mm light tube and an infrared detector

## 5 Conclusion

In this chapter, CMOS-compatible $CO_2$ sensors based on thermal-conductivity measurement have been presented. They detect the $CO_2$-dependent thermal conductivity of ambient air by measuring the heat loss of a suspended hot-wire transducer, realized in the VIA layer of a standard CMOS process to reduce fabrication cost and complexity. Two sensor designs have been presented, based on different readout approaches. The first approach is amplitude-domain TC sensing, which measures the steady-state temperature and power of a resistive transducer using a dual-mode incremental $\Delta\Sigma$ ADC. The second approach is time-domain TC sensing, which measures the phase shift of the temperature transients of a periodically heated transducer using a phase-domain $\Delta\Sigma$ ADC. Both approaches have been validated and proven to be capable of measuring $CO_2$ concentration with a resolution suitable for indoor air-quality monitoring. The time-domain approach achieves best-in-class energy efficiency. These results make the design a promising alternative to NDIR-based $CO_2$ sensors, especially in cost- and energy-constrained applications.

**Acknowledgments** This work was in part supported by NXP Semiconductors, The Netherlands, and in part by ams AG, The Netherlands. The authors want to thank Lukasz Pakula and Zu-yao Chang for their technical support.

## References

1. Emmerich SJ, Persily AK. Literature review on $CO_2$-based demand-controlled ventilation. ASHRAE Trans. 1997;103:229–43.
2. SenseAir K30 datasheet, SenseAir [Online]. Available: http://www.senseair.com/.
3. SGX Sensortech IR11BD datasheet, SGX Sensortech [Online]. Available: http://www.sgxsensortech.com/.

4. Frodl R, Tille T. A high-precision NDIR $CO_2$ gas sensor for automotive applications. IEEE Sensors J. 2006;6(6):1697–705.
5. Cai Z, et al. A ratiometric readout circuit for thermal-conductivity-based resistive $CO_2$ sensors. IEEE J Solid-State Circuits. 2016;51(10):2463–74.
6. Kliche K, et al. Sensor for thermal gas analysis based on micromachined silicon-microwires. IEEE Sensors J. 2013;13(7):2626–35.
7. Kliche K, et al. Sensor for gas analysis based on thermal conductivity, specific heat capacity and thermal diffusivity. In: Proceedings of IEEE international conference on MEMS. 2011 p. 1189–92.
8. XEN-5310 datasheet. Xensor Integration [Online]. Available: http://www.xensor.nl/.
9. Cai Z, et al. A phase-domain readout circuit for a CMOS-compatible hot-wire $CO_2$ sensor. IEEE J. Solid-State Circuits. (in press) doi: 10.1109/JSSC.2018.2866374
10. Simon I, Arndt M. Thermal and gas-sensing properties of a micromachined thermal conductivity sensor for the detection of hydrogen in automotive applications. Sens. Actuators A: Phys. 2002;97–98:104–8.
11. Ali SZ, et al. Tungsten-based SOI microhotplates for smart gas sensors. J Microelectromech Syst. 2008;17:1408–17.
12. Cai Z, et al. An integrated carbon dioxide sensor based on ratiometric thermal-conductivity measurement. In: Proceedings of IEEE international conference on solid-state sensors, actuators and microsystems (Transducers '15). 2015. p. 622–5.
13. Bult K, Geelen GJGM. A fast-settling CMOS op amp for SC circuits with 90-dB DC gain. IEEE J Solid-State Circuits. 1990;25(6):1379–84.
14. Fiedler H, et al. A 5-bit building block for 20 MHz A/D converters. IEEE J Solid-State Circuits. 1981;16(3):151–5.
15. FIGARO TGS8100 datasheet (rev06), FIGARO [Online]. Available: http://www.figaro.co.jp/.
16. Mahdavifar A, et al. Transient thermal response of micro-thermal conductivity detector (μTCD) for the identification of gas mixtures: an ultra-fast and low power method. Microsyst Nanoeng. 2015;1:15025.
17. van Vroonhoven C, de Graaf G, Makinwa KAA. Phase readout of thermal conductivity-based gas sensors. In: Proceedings of IEEE International Workshop on Advances in Sensors and Interfaces (IWASI). 2011. p. 199–202.
18. van Vroonhoven CPL, Makinwa KAA. A thermal-diffusivity-based temperature sensor with an untrimmed inaccuracy of ±0.5°C (3σ) from –40 to 105°C. In: Digest ISSCC. 2008. p. 576–7.
19. Kashmiri M, Xia S, Makinwa KAA. A temperature-to-digital converter based on an optimized electrothermal filter. IEEE J Solid-State Circuits. 2009;44(7):2026–35.
20. Kashmiri SM, Souri K, Makinwa KAA. A scaled thermal-diffusivity-based 16 MHz frequency reference in 0.16 μm CMOS. IEEE J Solid-State Circuits. 2012;47(7):1535–45.
21. Vincent TA, Gardner JW. A low cost MEMS based NDIR system for the monitoring of carbon dioxide in breath analysis at ppm levels. Sens Actuators B Chem. 2016;236:954–64.